Cross-comparison of global simulation models applied to Mercury's dayside magnetosphere

Sae Aizawa, Léa Griton, Shahab Fatemi, Willi Exner, Jan Deca, Filippo Pantellini, Manabu Yagi, Daniel Heyner, Vincent Génot, Nicolas André, et al.

Cross-comparison of global simulation models applied to Mercury's dayside magnetosphere

S. Aizawa[a,b,*], L. S. Griton[a,k], S. Fatemi[c,d], W. Exner[e,f,g], J. Deca[h,i,j], F. Pantellini[k], M. Yagi[l], D. Heyner[e], V. Génot[a], N. André[a], J. Amaya[m], G. Murakami[n], L. Beigbeder[o], M. Gangloff[a], M. Bouchemit[a], E. Budnik[p], H. Usui[q]

[a] *IRAP, CNRS-CNES-UPS, Toulouse, France*
[b] *Graduate School of Science, Tohoku University, Sendai, Japan*
[c] *Swedish Institute of Space Physics, Kiruna, Sweden*
[d] *Department of Physics at Umeå University, Umeå, Sweden*
[e] *Institute for Geophysics and extraterrestrial Physics, Technische Universität Braunschweig, Braunschweig, Germany*
[f] *Institute for Theoretical Physics, Technische Universität Braunschweig, Braunschweig, Germany*
[g] *School of Earth and Atmospheric Sciences, Georgia Institute of Technology, Atlanta, USA*
[h] *Laboratory for Atmospheric and Space Physics (LASP), University of Colorado Boulder, Boulder, Colorado 80303, USA*
[i] *Institute for Modeling Plasma, Atmospheres and Cosmic Dust, NASA/SSERVI, California 94035, USA*
[j] *Laboratoire Atmosphères, Milieux, Observations Spatiales (LATMOS), Université de Versailles à Saint Quentin, 78280 Guyancourt, France*
[k] *LESIA, Observatoire de Paris, Université PSL, CNRS, Sorbonne Université, Université de Paris, 5 place Jules Janssen, 92195 Meudon, France*
[l] *RIKEN, Kobe, Japan*
[m] *CmPA, Mathematics Department, KU Leuven, Belgium*
[n] *ISAS/JAXA, Sagamihara, Japan*
[o] *GFI, Toulouse, France*
[p] *Noveltis, Toulouse, France*
[q] *Kobe University, Kobe, Japan*

Abstract

We present the first comparison of multiple global simulations of the solar

*Corresponding author.
Email address: sae.aizawa@irap.omp.eu (S. Aizawa)

wind interaction with Mercury's dayside magnetosphere, conducted in the framework of the international collaborative project SHOTS - Studies on Hermean magnetosphere Oriented Theories and Simulations. Two magneto-hydrodynamic and two hybrid simulation codes are used to investigate the global response of the Hermean magnetosphere to a northward-oriented interplanetary magnetic field. We cross-compare the results of the four codes for a theoretical case and a MESSENGER orbit with similar upstream plasma conditions. The models agree on bowshock and magnetopause locations at 2.1 ± 0.1 and 1.4 ± 0.08 Mercury planetary radii, respectively. The latter locations may be influenced by subtle differences in the treatment of the plasma boundary at the planetary surface. The predicted magnetosheath thickness varies less between the codes. Finally, we also sample the plasma data along virtual trajectories of BepiColombo's Magnetospheric and Planetary Orbiter. Our ability to accurately predict the structure of the Hermean magnetosphere aids the analysis of the onboard plasma measurements of past and future magnetospheric missions.

Keywords: Mercury, BepiColombo, Modeling

1. Introduction

Mercury is a planet of extremes that is continuously battered by a harsh and dynamic solar wind. Combined with interplanetary magnetic field (IMF) magnitudes up to 30 nT and a small Parker spiral angle, Mercury's weak internal magnetic field produces a unique magnetosphere in the solar system [1, 2, 3, 4, 5]. For example, the Hermean magnetosphere is twenty times smaller in volume than Earth's magnetosphere and Mercury's volume frac-

tion in its magnetosphere is approximately five hundred times larger than the equivalent terrestrial number. As a result, the solar wind can directly interact with the surface, even outside the magnetospheric cusps [6]. In addition, the significant offset between the magnetic dipole origin and the center of the planet results in a surface magnetic field strength in the northern hemisphere that is double the nominal value estimated for the southern hemisphere [7, 8, 9]. These particularities culminate in fascinating particle precipitation patterns and differential space weathering that is as variable as the upstream solar wind [10, 11, 12]. The absence of a significant ionosphere makes Mercury's conductive core an integral part of the electrodynamic current closure and complicates the evolution of the complex local plasma environment even more [13, 14].

Numerical simulations of the solar wind interaction with the Hermean magnetosphere have thus far adopted multi-fluid/magnetohydrodynamic [15, 16, 17, 18] and hybrid approaches (representing the ions as computational particles and the electron populations as a (massless) fluid) [19, 20, 21, 22, 23, 24, 25, 26, 12]. These models, designed to focus on the ion kinetics, have been successful in recreating the general structure of Mercury's local plasma environment. For example, with a hybrid model Müller et al. [27] characterised a diamagnetic current system that originates from the proton pressure gradients at Mercury's inner magnetosphere to explain the day- and night-side diamagnetic decreases observed by MESSENGER [28, 29]. In addition, recent numerical developments have produced the first fully kinetic, global simulations of the Hermean magnetosphere [30, 31, 32].

Due to mission constraints, both the Mariner-10 and MESSENGER spacecraft were limited to measure the Hermean plasma environment and thus, to fully disentangle plasma processes such as finite-gyroradius effects and complex electron dynamics [4]. Complementary to the previous missions, BepiColombo's Magnetospheric (Mio) [33]) and Planetary Orbiter (MPO) [34]) allow for multi-spacecraft coordinated observations. Their plasma instruments focus on direct measurements of the response of Mercury's magnetosphere and its near-space environment to dynamic changes in the solar wind, including plasma-wave-charged-particle resonances, kinetic-scale instabilities and particle distributions, and energy transfer via field-aligned currents and waves [4].

In order to optimally prepare for the measurement campaign and to be able to fully interpret and analyse the data during the forthcoming Mercury flybys and during the orbital phase, or in other words, to exploit most efficiently the multi-point measurements allowed by the dual spacecraft and the synergies between the various sensors of the onboard plasma suite, sophisticated modelling tools are required. Hence, the SHOTS (Studies on Hermean magnetosphere Oriented Theories and Simulations) project has been established as an integral part of the BepiColombo Young Scientist Working Group. Its aim is to share and compare simulations results among the BepiColombo Science Working Team in order to prepare the scientific analysis of the in-situ magnetospheric observations gathered by Mio and MPO.

In this first comparative study, we identify the differences between fluid and hybrid simulation approaches to model the structure of the Hermean magnetosphere and its plasma environment. We compare the bow shock and magnetopause locations with a representative set of MESSENGER measurements and predict the plasma environment along virtual trajectories of BepiColombo's Mio and MPO spacecraft.

2. Model descriptions and methodology constraints

The four computer models used in this comparison study are briefly described here, with special emphasis on their inner boundary conditions. We find that subtle differences in the treatment of the plasma boundary at the planetary surface affect the global solar wind - magnetosphere structure. Two magnetohydrodynamic (MHD) and two hybrid codes have been employed to identify the consequences of the different assumptions that are implemented in the physical model of the codes. In Table 1, we summarize the general numerical settings adopted for the four codes, such as the number of cells used, the size of the simulation domain and the spatial resolution. The output from all models are stored and discussed using the Mercury Solar Orbital (MSO) frame. The X-axis points towards the Sun and the Y-axis is chosen opposite to the orbital motion of Mercury. The Z-axis points to the geophysical north and completes the right-handed coordinate system. The intrinsic magnetic field of the planet is set as a dipole with a 480 km offset towards the north from the planetary center [35]. The dipole moment is $200\,\mathrm{nT} \times \mathrm{R_M^3}$. To avoid further numerical complexities, we do not include the tenuous Mercury's ex-

osphere in our simulations just yet.

2.1. MHD models

The three-dimensional MPI-AMRVAC code (hereafter AMRVAC) integrates the MHD equations using a two-step Lax-Friedrichs-type scheme associated with a Woodward gradient limiter [36, 37]. A Powell correction is also used to satisfy the $\nabla \cdot \mathbf{B} = 0$ condition at each time step [38]. In order to limit magnetic diffusion, the magnetic field $\mathbf{B}$ is split into an analytically prescribed background field $\mathbf{B_0}$ and a residual field $\mathbf{B_1}$ [39]. The full system of equations is solved on a spherical grid that is linearly spaced along the angular coordinates θ and ϕ and logarithmically spaced along the radial coordinate r. Hence, the simulation domain itself is a spherical shell. At the outer boundary, free slip conditions ($\partial/\partial r = 0$) are applied to all fields where the angle between the solar wind direction and the normal to the boundary direction is $< 80°$. Ambient (upstream) solar wind conditions are set at the remaining sides of the domain. At the inner boundary of the simulation domain, here the planetary surface, the radial velocity is set to zero. A free slip condition is applied to the tangential components of the momentum $\rho\mathbf{v}$. If the radial velocity immediately above the surface is positive (i.e. in case of outflow), the plasma number density and the total fluid pressure are set to $n_p = n_e = 15\,\mathrm{cm}^{-3}$ and $p = 0.1\,\mathrm{nPa}$, respectively. On the other hand, if the radial velocity immediately above the surface is negative (i.e. in case of inflow), n_p and p are allowed to float within 15 - $150\,\mathrm{cm}^{-3}$ and 0.1 - 1 nPa. A free slip condition is also applied to the normal component of $\mathbf{B_1}$ at the surface. The tangential components are set to zero.

Note from Table 1 that only AMRVAC employs a spherical coordinate system. With a total number of cells of $(N_r, N_\theta, N_\phi) = (36, 36, 72)$, covering the radial interval $r \in R_{\rm M}\,[1, 10]$, the horizontal and vertical cell size near the surface are 213 km and 161 km, respectively. Postmortem, the results of AMRVAC are interpolated to a uniform Cartesian grid with a spatial resolution of 81.5^3 km^3 for ease of comparison with the other simulation models.

YAGI's code is the second three-dimensional MHD model we use [40, 41]. In contrast to AMRVAC, a uniform Cartesian grid is adopted and the vector potential $\mathbf{A}$ is computed instead of the magnetic field, ensuring $\nabla \cdot \mathbf{B} = 0$ by definition. In addition, a Rational-CIP algorithm is implemented to solve the advection term [41]. A fourth-order Runge Kutta and a fourth-order central difference method are used to solve the non-advection terms needed to advance the numerical scheme in time and space. The inner boundary of the computational domain is the planetary surface. Mercury is treated as a reflective obstacle, allowing no flux to penetrate across the surface (obstacle). We also do not allow any radial pressure and density gradient at the planetary surface. The inner boundary conditions accommodate a smooth convection of the magnetic field in the vicinity of the planet, mimicking obstacle with low conductivity.

2.2. Hybrid models

AIKEF (Adaptive Ion Kinetic Electron Fluid) is a hybrid code that operates on a Cartesian grid. The mesh is capable of automatically adapting its resolution in regions where large field gradients exist [42, 26]. For simplicity,

we do not activate this function here and use a fixed spatial resolution of $100\,\mathrm{km}^3$ instead. Contrary to MHD, a hybrid model treats ions kinetically and uses computational macro-particles to represent their velocity distribution. The number of macro-particles per cell is set to 25 to describe the initial Maxwellian distribution. Electrons are included as a massless charge-neutralizing fluid. To include induction effects, a radial resistivity profile is applied. The maximum resistivity is set to $1.21 \times 10^7\,\Omega\,m$ within the mantle [17]. Mercury's surface is treated as a perfect plasma absorber, i.e., particles impacting the surface are removed. Within the vacuum regions of the nightside magnetosphere, ghost-particles with the same charge-to-mass ratio as the upstream solar wind protons are inserted to allow local magnetic field diffusion. Their density is tenuous so that no physical feedback onto the dynamics of the magnetosphere is present. A 2% smoothing parameter is applied between the grid points to ensure numerical stability [43].

The Amitis (advanced modeling infrastructure in space simulations) is a GPU-based (Graphics Processing Units) three-dimensional hybrid model of plasma that currently runs only on a single CPU-GPU pair. It has been developed to reduce the computational resources that are typically needed for running global simulations and resulted in performance enhancement of 10x-100x over its CPU-based predecessor [24]. The model kinetically tracks positively charged macro-particles, i.e., the ion population, by solving the Lorentz equation of motion while using a fluid description for mass-less electrons. The electric field $\mathbf{E}$ is directly calculated from the electron momentum equation and Faraday's law, $\partial\mathbf{B}/\partial t = -\nabla \times \mathbf{E}$, is used to advance the mag-

netic field $\mathbf{B}$ in time. The model is grid-based and uses regular-spaced, cell-center Cartesian grids to solve all the equations. We choose a spatial resolution of $170\,\mathrm{km}^3$ with 12 macro-particles per cell. The model self-consistently couples the geophysical, induced electromagnetic response of the interior of a planetary body to the electromagnetic response of the incident plasma and magnetic fields by solving Maxwell's equations for the plasma and a magnetic diffusion equation ($\partial\mathbf{B}/\partial t = -\nabla \times \nabla \times \mathbf{B}/\mu_0\sigma$) for the interior of an object, where μ_0 is the permeability of free space and σ is the conductive profile for the interior of the planetary body [24]. When a particle impacts the planetary surface, it is removed from the simulation domain.Vacuum regions that form within the computational domain are assumed a resisitivity $10^7\,\Omega\,\mathrm{m}$. Note that AIKEF uses ghost particles instead. Amitis adopts periodic outer boundary conditions for its particles and electromagnetic fields along the axes perpendicular to the solar wind flow. Parallel to the flow the code continuously injects solar wind ions at the most upstream grid cell. The downstream boundary, identical to its implementation of the planetary surface, is a perfect plasma absorber.

2.3. Common visualization tools

We use netCDF as a multidimensional format with meta information for all simulations. It allows us to have a unified format for comparative visualizations, data interoperability and reusability. In the present study, we employ Paraview for 3D data visualization and analysis. In addition, we use 3Dview and AMDA, which makes use of the SPASE simulation data model [44, 45, 46, 47]. Using SPICE kernels, 3Dview is a 3D JAVA tool that

	Grid type	#cells	Domain size	Resolution	particles/cell
AMRVAC	Spherical	(36, 36, 72)	$r \in R_{\rm M}\,[1, 10]$	$213 \times 161\,$km	-
YAGI	Cartesian	(300, 300, 300)	(-10:+6,$\pm$5,$\pm$5) $R_{\rm M}$	122 km	-
AIKEF	Cartesian	(320, 224, 224)	(-6:+8,$\pm$9,$\pm$9) $R_{\rm M}$	100 km	25
Amitis	Cartesian	(180, 280, 280)	($\pm$7,$\pm$10,$\pm$10) $R_{\rm M}$	170 km	12

Table 1: Summary of the numerical settings. For AMRVAC the finest spatial resolution is quoted.

provides visualizations of the positions and attitudes of planetary missions and bodies in combination with observational data, simulations, and analytical models. AMDA is an online database and analysis tool in which in-situ observations, ground based observations, and models can be browsed, manipulated and downloaded (a workspace is available for each user). AMDA and 3Dview are developed by the CDPP (Centre de Données de la Physique de Plasmas) and available to contributing developers under a GPLv3 licence.

3. Science cases

In this work we discuss two cases: (a) a classical textbook case under purely northward IMF conditions, and (b) a direct comparison with a preselected MESSENGER orbit.

3.1. Case a: Northward IMF

Northward IMF conditions are chosen to anticipate a stable dayside magnetosphere structure. Typically, a southward IMF gives rise to more unstable magnetosphere conditions as continuous dayside magnetic reconnection in

combination with a relatively short Dungey cycle does not allow the system to relax in between [8]. In the case of a northward IMF, the reconnection sites move to high latitudes near the magnetospheric cusps.

We set the IMF magnitude to 20 nT and adopt a solar wind proton density of 30 cm^{-3}, an Alfvén Mach number of 5 and a total plasma beta (β) of 1.3. The solar wind speed measures 400 $\mathrm{km\,s}^{-1}$ [48, 6]. The MHD models assume a total density equal to the proton density, whereas the plasma temperature (43 eV) is set to the sum of the electron (21.5 eV) and proton (21.5 eV) temperatures (Table 2).

3.2. Case b: MESSENGER comparison

We select a MESSENGER orbit that allows a simulation setup as close as possible to our theoretical northward IMF case. Due to its mid-day to midnight orientation (X-Z plane), orbit 1415 (November 8, 2012) provides a close comparison. The orbit has a Disturbance Index of less than 25 [49], the lowest magnetic activity quartile, the Z-components of the IMF at the inbound an outbound bow shock crossings are positive and within 2 nT of each other, and the IMF variability along the entire orbit is less than 10 nT. Combined these parameter values indicate stable solar wind conditions.

We use the inbound part of the orbit to compute the average IMF vector to be inserted in our models. Further, the Alfvén Mach number is set to 5, the solar wind speed equals 459 $\mathrm{km\,s}^{-1}$ and the proton and electron temperature measure 12 eV, and 18 eV, respectively [50, 51].

Table 2: Summary of the common input plasma parameters. *SW* denote the solar wind.

	Northward case	MESSENGER case
Planetary radius R_M [km]	2440	2440
Planetary dipole moment [nT $\times R_M^3$]	200	200
Northward dipole offset [km]	480	480
SW proton density [cm^{-3}]	30	40
SW proton + electron temperature [eV]	21.5+21.5	12+18
SW total plasma β	1.3	0.69
SW Alfvén Mach number	5	5
SW plasma velocity [$km\,s^{-1}$]	400	459
SW Sonic Mach number	6.8	8.5
IMF (X,Y,Z) components [nT]	(0, 0, +20)	(25, -6, 4.9)

4. Results

4.1. Case a: Northward IMF

A purely northward IMF configuration provides a stable magnetosphere configuration. We find that all simulation models reach quasi-steady state after roughly 300 seconds. Figure 1 shows the solar wind proton density maps in the $X-Z$ plane on a logarithmic scale, including also magnetic field lines. The two left panels are the results from the MHD codes while the two right panels present the results from the hybrid codes. All models have converged to a very similar global structure for the Hermean magnetosphere and the characteristic feature are present: the shape of bowshock, the higher density magnetosheath, and the magnetospheric cusps. However, the models do not agree on the proton density near the planet and inside the nightside magne-

tosphere. We also observe different locations of the magnetopause structure.

AMRVAC (Figure 1, upper left panel) shows a less sharp shock structure at the bow shock, a low density dayside magnetosphere, patches of higher density close to the surface in the cusp and tail regions, and an asymmetric (southward) magnetic field structure for the nightside magnetosphere. The latter is uniquely present in AMRVAC. The model also has the largest magnetopause flaring angle among the four models. YAGI's MHD code (bottom left panel) presents a sharper bow shock as compared to AMRVAC, most likely due to the model's less diffusive scheme. In addition, the dayside magnetosphere is not dilute and houses a similar density as the magnetosheath. The nightside structure of the magnetic field is more symmetric and slightly tilted northward. The density concentration we find near the tail region in the AMRVAC model is not present here. Finally, only YAGI's model results show a north-south symmetric cusp region. AIKEF (upper right panel), similar to AMRVAC and Amitis, produces a sharp bowshock and a more dilute dayside magnetosphere region. Both hybrid codes concur on narrower cusps as compared to the MHD models. The nightside magnetic field structure is tilted slightly northward, similar to YAGI's model. Note that upstream of the magnetosphere the magnetic field lines are curved due to the numerical smoothing algorithm AIKEF applies. Amitis (bottom right panel) does not employ any smoothing routines. Operating with a lower number of particles per cell as compared to AIKEF, the density maps therefore seem to contain more numerical noise. However, the bowshock and magnetopause are clearly captured and the solar wind plasma is denied from penetrating through the

dayside magnetosphere. The narrow cusp structure is similar to the results from AIKEF. The magnetic field configuration at the nightside of the planet is most symmetric. Amitis computes the lowest density in the magnetotail of our four models because the model does not depend on ghost particles in the lowest density areas of the simulation domain.

In order to quantify the differences between the four models, Figure 2 presents the pressure profile along the subsolar line (X-axis). The dynamic and magnetic pressure are extracted and the locations of the bowshock and magnetopause have been identified. The four panels correspond to the four simulations. The solid lines show the dynamic (ram) pressure, $\varrho \mathbf{v}^2$, while the dashed lines represents the magnetic pressure, $B^2/2\mu$. The gray dash-dotted line is the magnetic pressure produced by an uncompressed dipole magnetic field with the same dipole moment as the models, providing information on how much the planetary magnetic field is compressed by the solar wind. The gray vertical line at $x = 1.12\,R_{\mathrm{M}}$ indicates the point where the dynamic pressure equals the uncompressed magnetic pressure and serves as a reference for the magnetopause location. For each model, the position of the bow shock (BS) has been identified as the maximum velocity and density gradient (red vertical solid line). The location of the magnetopause (MP; red vertical dashed line) has been identified in three different ways: (1) using the position of the most distant closed planetary field line that crosses the X-axis, (2) using the position where the gas and magnetic pressure are equal, and (3) using the position where the current density has its maximum. All three methods were in excellent agreement for all four models (Table 3).

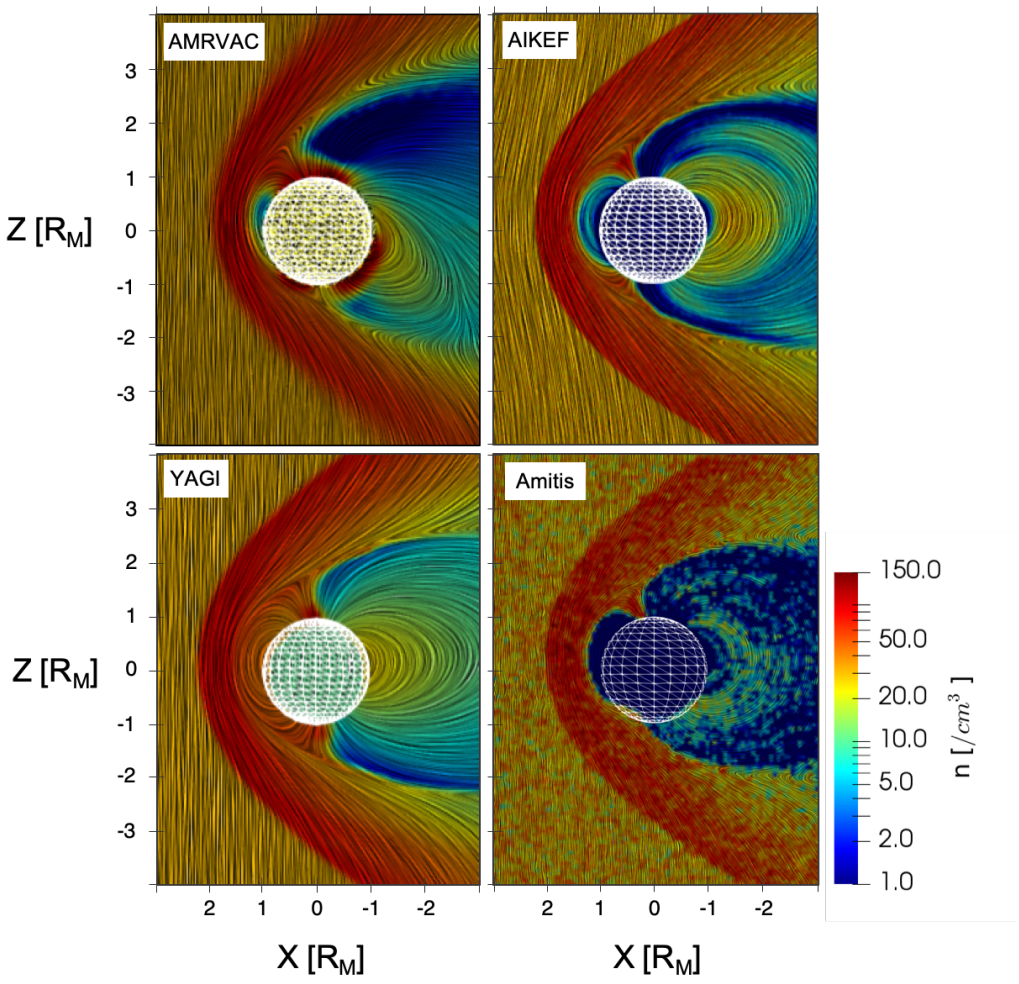

Figure 1: Maps of the solar wind proton density in the X-Z plane at steady-state for the four simulation models. The panels on the left (right) are the results from the MHD (hybrid) codes. Length scales are normalized to the Mercury radius.

Table 3: Summary of the bow shock and magnetopause locations, and the thickness of the magnetosheath for the four simulation models.

		BS [R_M]	MP [R_M]	Sheath thickness [R_M]
MHD	AMRVAC	1.99	1.30	0.69
	YAGI	2.21	1.50	0.71
Hybrid	AIKEF	2.18	1.42	0.76
	Amitis	2.22	1.48	0.74
	Mean value	2.14	1.41	0.73
Standard Deviation		0.094	0.078	0.027

285

286 The locations of both the bow shock and magnetopause vary among the
287 models with a range of $0.23\,R_M$ and $0.2\,R_M$, respectively (Figure 2 and Ta-
288 ble 3). The mean position of the bow shock and magnetopause is found at
289 $2.15\,R_M$, and $1.41\,R_M$, with a standard deviation of $\sigma = 0.094$ and $\sigma = 0.078$.
290 The variation of the magnetopause location is greater than that of the bow
291 shock as the former is more sensitive to the boundary condition applied at
292 the surface and inside the planet. In effort to eliminate the effects of the
293 numerical implementation for comparison purposes, we compute the average
294 thickness of the magnetosheath and find $0.73\,R_M$ with a standard deviation
295 of 0.027. We find that the hybrid models predict a slightly thicker magne-
296 tosheath as compared to the MHD models. Note that the mean BS and MP
297 locations simulated here with a purely northward IMF are within the ranges
298 measured by MESSENGER [6].

299

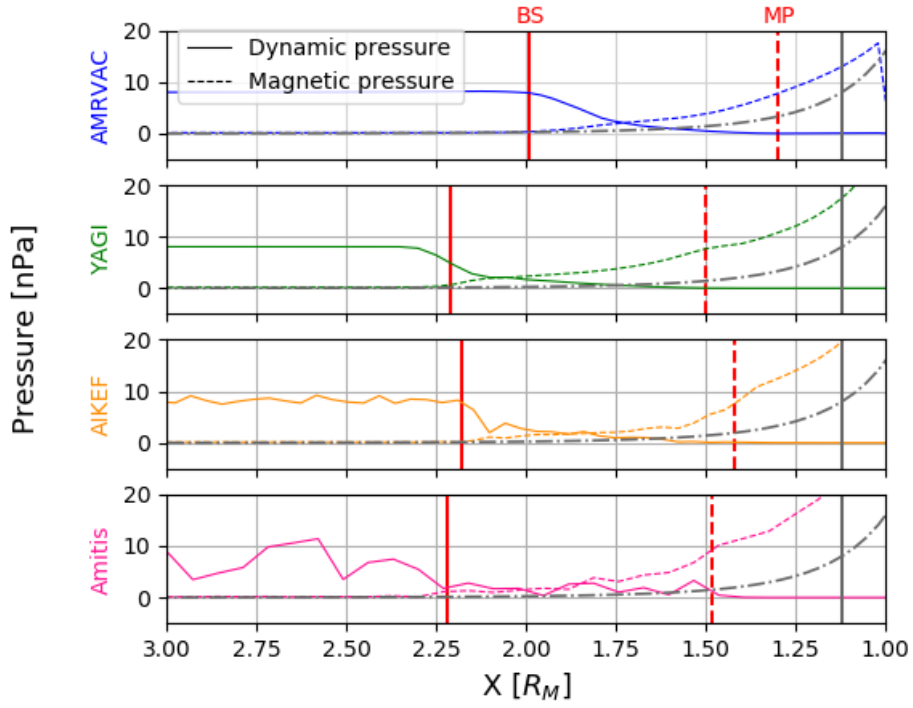

Figure 2: Dynamic (ram) and magnetic pressure profiles along the X-axis (Sun-Mercury direction) from 3 R_{M} upstream to the planet surface on the dayside for the four simulation codes. The results from the two MHD codes are shown on the top two panels and the hybrid model results on the two bottom panels. The gray dash-dotted line is the magnetic pressure produced by an uncompressed dipole magnetic field with the same dipole moment as the models. The positions of the bow shock (BS) and magnetopause (MP) are shown with red vertical solid and dashed lines. The grey vertical line gives the theoretical expected position of the magnetopause.

In addition to the bow shock and magnetopause locations along the sub-solar line, we further characterize the Hermean magnetosphere by means of the reconnection sites. Figure 3 shows a map in the X-Z plane with its origin at the center of the planet. For reference, the two gray dashed lines represent the bow shock and magnetopause locations as predicted by the models of Slavin et al. [52], Shue et al. [53], Winslow et al. [6]. The positions of the reconnection site, i.e. the null points, identified from the simulated magnetic field structure by our four models are indicated with full colored circles. The locations of the magnetopause at $X = -2\,R_M$ are represented with colored crosses. On average, the null points near the northern cup are located more towards the nightside, whereas the null point near the southern cusp are clustered more towards the terminator plane (with exception of YAGI's model). Due to the dipole offset towards the north, the southern null points are closest to the planet. Note that apart from the chosen plasma field conditions also various code-specific parameters, such as numerical resistivity, may play a role in where the reconnection sites develop. AMRVAC shows the largest north-south asymmetry on the location of null points, which is consistent with the tilted magnetic structure seen in Figure 1. The locations of the magnetopause on the nightside of the planet are obtained from the gradients of the density and the current density. With the exception of AMRVAC, these are located within the reference magnetopause model ($R_{ss} = 1.45\,R_M$ and $\alpha = 0.5$ [53, 6]). Given the purely northward IMF, all four simulations can be considered in good agreement with the reference models.

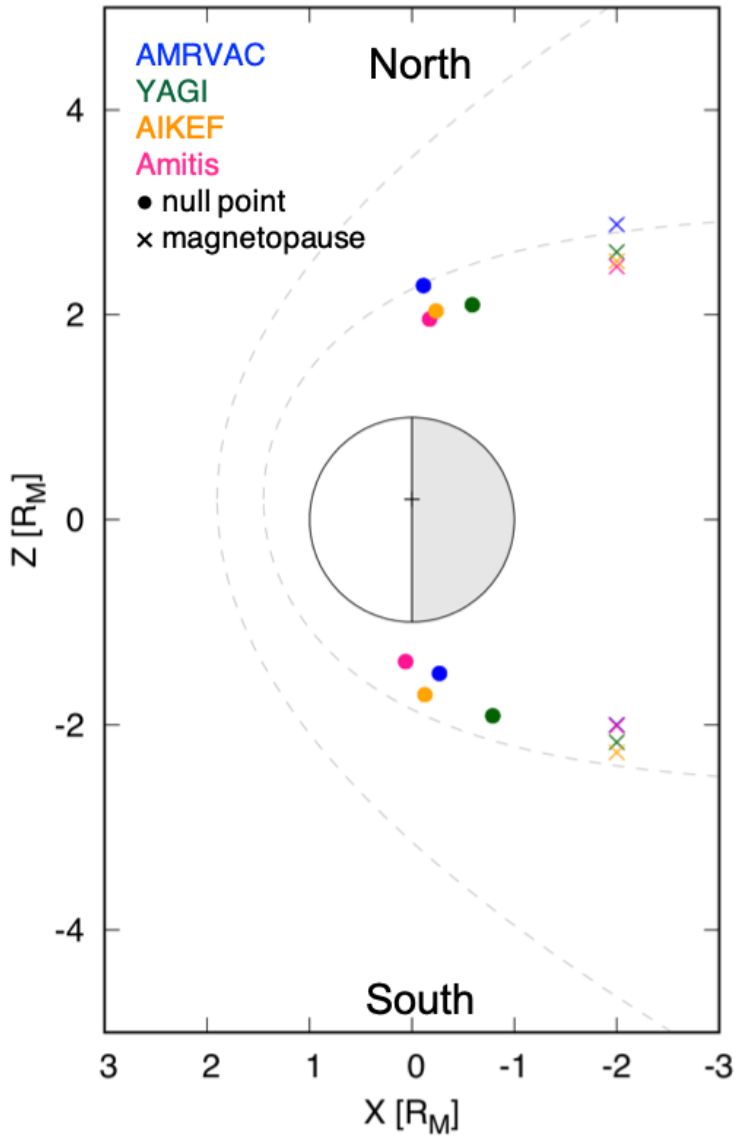

Figure 3: The locations of null points (colored circles) and magnetopause (colored crosses) in the X-Z plane. The dashed lines show the bow shock and magnetopause models defined by Slavin et al. [52] and Shue et al. [53], respectively. The magnetopause paraboloid has parameters $R_{ss} = 1.45\,R_{\rm M}$ and $\alpha = 0.5$. The bow chock model parameters are $p = 2.75\,R_{\rm M}$, $\epsilon = 1.04$, and $X_0 = 0.5\,R_{\rm M}$.

4.2. Case b: MESSENGER comparison

Figure 4 presents the magnetic field, density and plasma velocity profile along MESSENGER orbit 1415 from 4:30 UT to 10:00 UT (see also section 3.2). The spacecraft entered the magnetosphere at the nightside along a south to north trajectory, roughly in the meridian plane with its closest approach near the magnetic north of Mercury, thus crossing the bow shock and magnetopause twice. Four vertical black lines indicate the bow shock and magnetopause locations for both the inbound and outbound crossings observed by MESSENGER. Superimposed on their respective panels are the simulated profiles from Case a along the same trajectory. The red vertical lines are the averaged simulated shock crossings from the four models. Overall, our models are in close agreement with the MESSENGER data for the inbound part of the orbit. With time differences of up to 12 min, equal to $\sim$0.28 R_M along the spacecraft trajectory for the inbound orbit, and 17 min ($\sim$1.1 R_M) for the outbound orbit, the locations of the BS and MP agree less well for the outbound section of the MESSENGER orbit. The BS locations match better for the inbound part of the orbit.

Since we used the inbound part of the orbit to constrain the upstream plasma parameters to initialize the simulations, it is possible that variations in the solar wind dynamic pressure during the orbit may be responsible for the larger discrepancy in the outbound part of the orbit. Interestingly, there are distinct differences between the MHD and the hybrid codes (panel 4 of Figure 4). Around 7:50 UT, when the spacecraft is inside the dayside magnetosheath, the results from the two hybrid simulations are in agreement

with the observations, while both MHD models predict a lower magnetic field intensity. The spacecraft passes through the northern cusp and then moves towards the dayside region. At 8:10 UT, near the peak density, we find the compressed magnetosheath plasma. As expected, also the density and velocity profiles predicted by the hybrid codes show steeper profiles at the shock crossing compard to the MHD models.

5. Discussion

Due to the limited particle instrumentation on board the single-spacecraft MESSENGER mission, it is not possible to constrain the exact solar wind plasma parameters to set up a comparison simulation. In addition, the solar wind varies in time and may even be changing significantly while MESSENGER crosses the mgnetosphere. This may be the reason for some of the discrepancies between simulated and measured profiles. In Figure 5 we compute the difference between the observed and modeled magnetic fields along our chosen MESSENGER orbit. We exclude the time frame between the two MP crossings (from 6:15 UT to 7:45 UT) while MESSENGER passed the nightside region of the magnetosphere, hence, focusing on the cusp and dayside region.

Just before 5:00 UT, MESSENGER crosses the BS for the first time, about 3 min before the predicted averaged time stamp from our models. Continuing along the trajectory, both the modeled X- and Z-component agree well with MESSENGER, whereas the models underestimate the magnetic

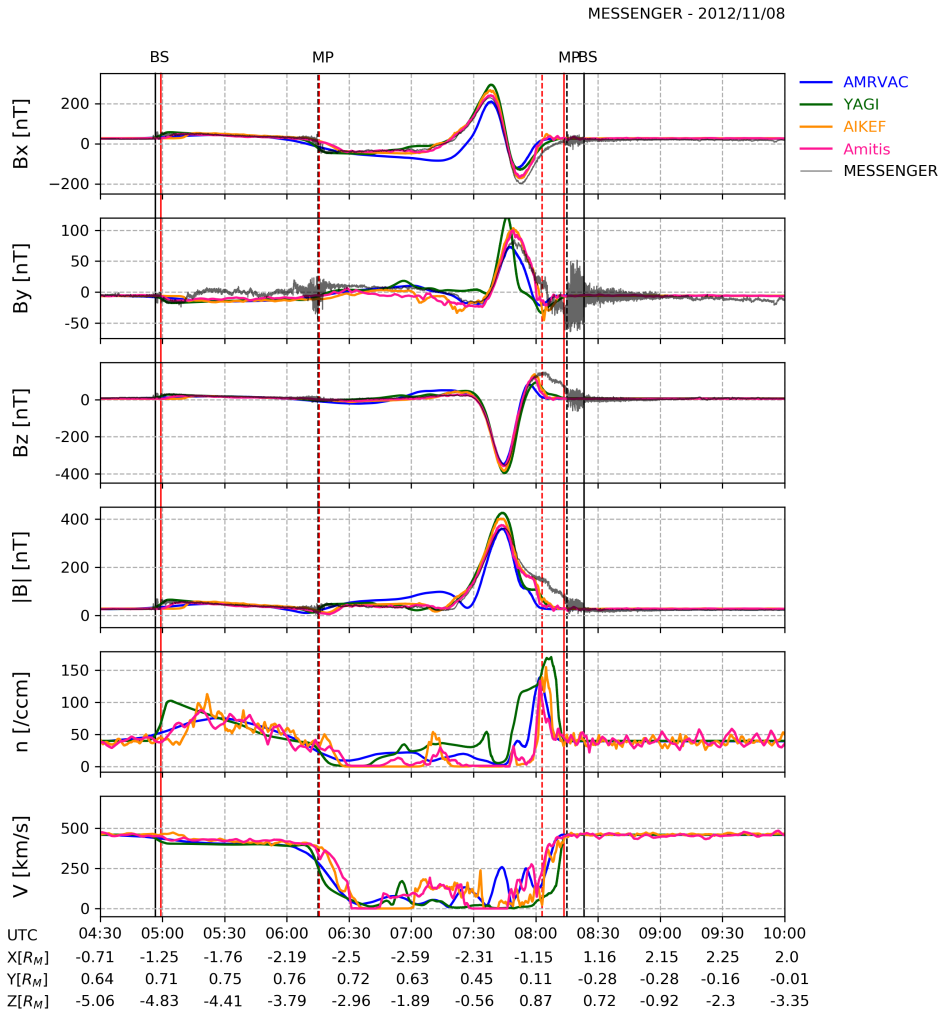

Figure 4: Modeled and observed magnetic field and modeled particle data along orbit 1415 of MESSENGER. Blue, green, orange, and red lines shows the results from AMRVAC, YAGI, AIKEF and Amitis, respectively. The black lines shows the magnetometer data measured by MESSENGER. The bow shock (BS) and magnetopause (MP) crossings identified from the observations are indicated using a vertical solid and dashed black line. The averaged simulated shock and magnetopause crossings are shown by red solid and dashed lines.

field contribution by roughly 15 nT along the Y direction. Our models agree on the inbound MP crossing time at 6:15 UT within a 5 min time range. At 7:50 UT, when MESSENGER moves from the nightside to the dayside in the northern hemisphere, all four models predict a magnetic pile-up, although none of the models fully reproduces the fine-scale structure. Immediately following the pile-up, the models underestimate the magnetic field strength by roughly 100 nT. Note that the different profiles in Figure 4 show no real 'winner' among the four simulation models as all codes show different small-scale discrepancies with the MESSENGER measurements at the boundaries between the distinct plasma regions of Mercury's magnetosphere. It shows the need for a multi-spacecraft mission, such as BepiColombo, to simultaneously measure the local Hermean and upstream plasma environment in order to fine-tune numerical models and in turn characterize Mercury's global plasma environment.

5.1. Virtual sampling along Mio/MPO orbits

One of the major goals of the SHOTS project, next to comparing different simulation approaches with available MESSENGER measurements, is to help prepare the community for the forthcoming BepiColombo mission by making available a catalog of simulation case that study the plasma structure and dynamics of Mercury's magnetosphere under different solar wind conditions. In the first step of this project, we chose four different (MHD and hybrid) simulation models. Figures 6 and 7 show the plasma characteristics expected along a typical Mio and MPO orbit, respectively, during the nominal orbital phase of BepiColombo. We chose the upstream solar wind

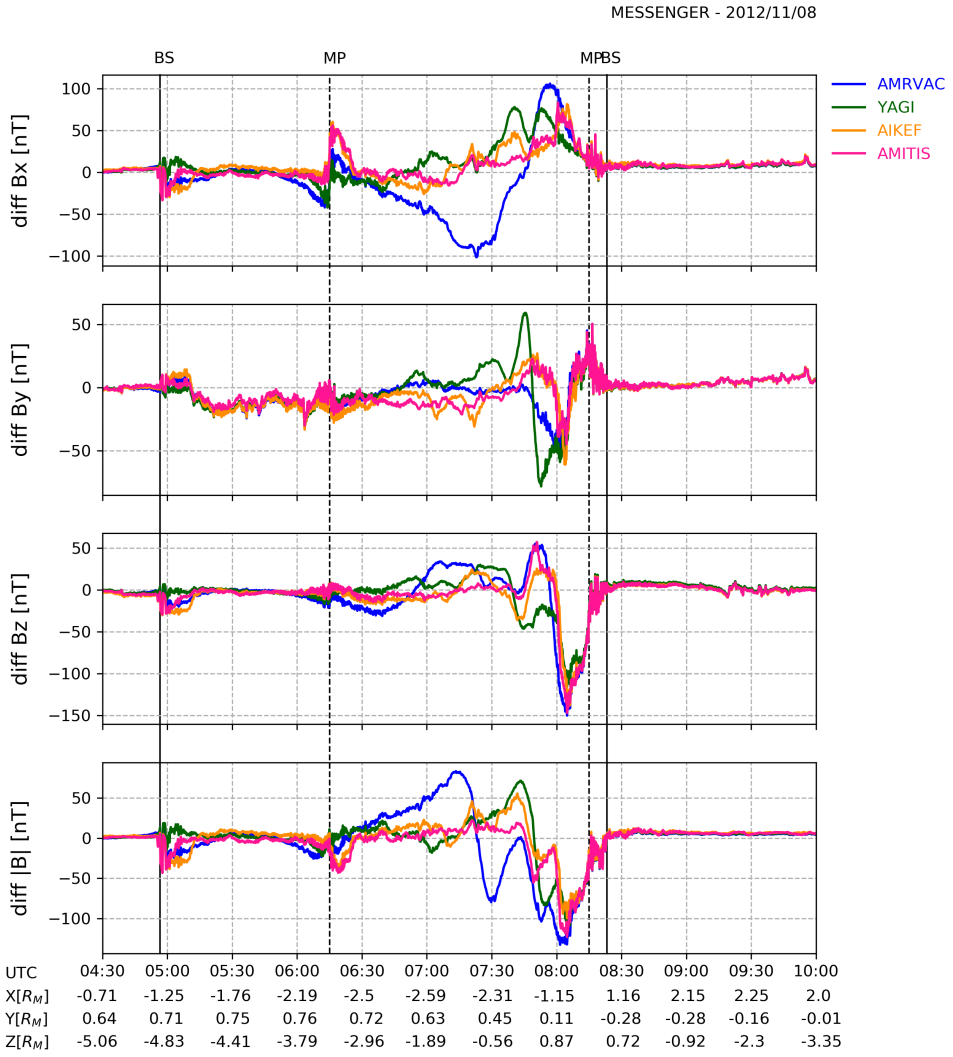

Figure 5: Difference between the simulation results and the MESSENGER magnetic field measurements. The bow shock (BS) and magnetopause (MP) crossings identified from the observations are indicated with a vertical solid and dashed line, respectively.

conditions identical to the MESSENGER case studied above (Table 2). For ease of comparison, the orbital plane is set perpendicular to the X direction, corresponding to BepiColombo's operations planned for April 4, 2026. During this period, both Mio and MPO remain inside the magnetosphere and the plasma environment will be fully observed by the magnetometers on board Mio and MPO [54, 55], the Mercury Plasma Particle Experiment (MPPE) [56] and the Plasma Wave Investigation (PWI) [57] onboard Mio, and the Search for Exospheric Refilling and Emitted Natural Abundances (SERENA) on board MPO [58].

In both Figures 6 and 7 the solid vertical lines indicate the southern (T_S) and northern (T_N) terminator crossing and the dashed vertical line is the time when the spacecraft crosses the sub-solar point (SSP). During this period, Mio will be moving along the frontside magnetopause (from 15:15 UT to 15:35 UT) where our models predict an enhancement of the magnetic field intensity and plasma velocity. Note that the predicted profiles closest to the planet are not in agreement, possibly due to the numerical treatment of the planetary boundary condition. Next, Mio will move across the cusp region and re-enter the nightside magnetosphere from the north. After crossing the northern terminator at 15:50 UT, the density and velocity profiles diverge. A similar trend is not visible in the magnetic field predictions. This may be the region where the ion dynamics has the largest impact, hence producing the largest differences between the hybrid and MHD models.

MPO will orbit significantly closer to the planet. The spacecraft will leave

the southern magnetosphere via the nightside, then crosses the terminator and enters the dayside magnetosphere. Just before 15:00 UT and around 15:35 UT, the two hybrid models predict a significant density enhancement, indicating the presence of trapped particles. The spacecraft passes through the cusp region (gray areas in Figure 7). MPO's trajectory will be most useful to better understand the structure and dynamics of the magnetosphere closest to the planet and in particular near the southern hemisphere. This region has been explored less due to MESSENGER's highly inclined and eccentric orbit.

Sampling the virtual orbits of Mio and MPO for a variety of solar wind parameters and/or models, we will be able to predict when the spacecraft most likely cross the cusp, the plasma sheet and the shocked regions within certain margins. These margins depend on the characteristics of the simulation and the physical processes included in the model. The combined measurements from the two spacecraft will provide a wealth of information on the Hermean plasma environment, making predictive simulations a necessity to maximize the scientific return of the mission. To this effect, the simulation domain needs to be extended farther downstream of the planet to capture better the magnetotail region. Also temporal information needs to be included. Finally, also simulation tools that include the electron dynamics are needed.

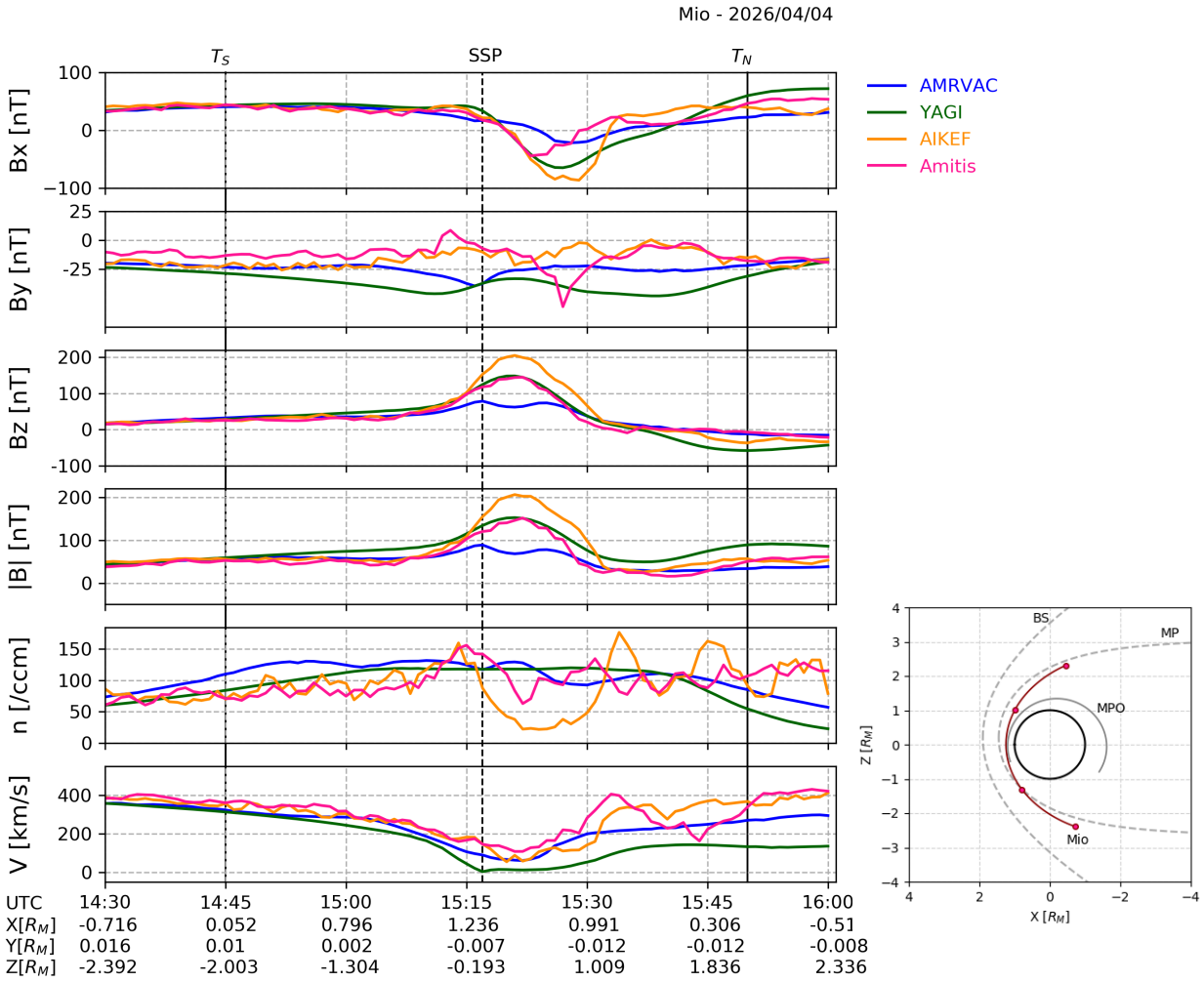

Figure 6: Magnetic field and particle data along a representative Mio orbit. The red dots along the trajectory in the inset panel show the position of the spacecraft along 30 min intervals. The solid vertical lines indicate the crossing of the southern (T_S) and northern (T_N) terminator, the dashed vertical line is the time when the spacecraft crosses the subsolar point (SSP).

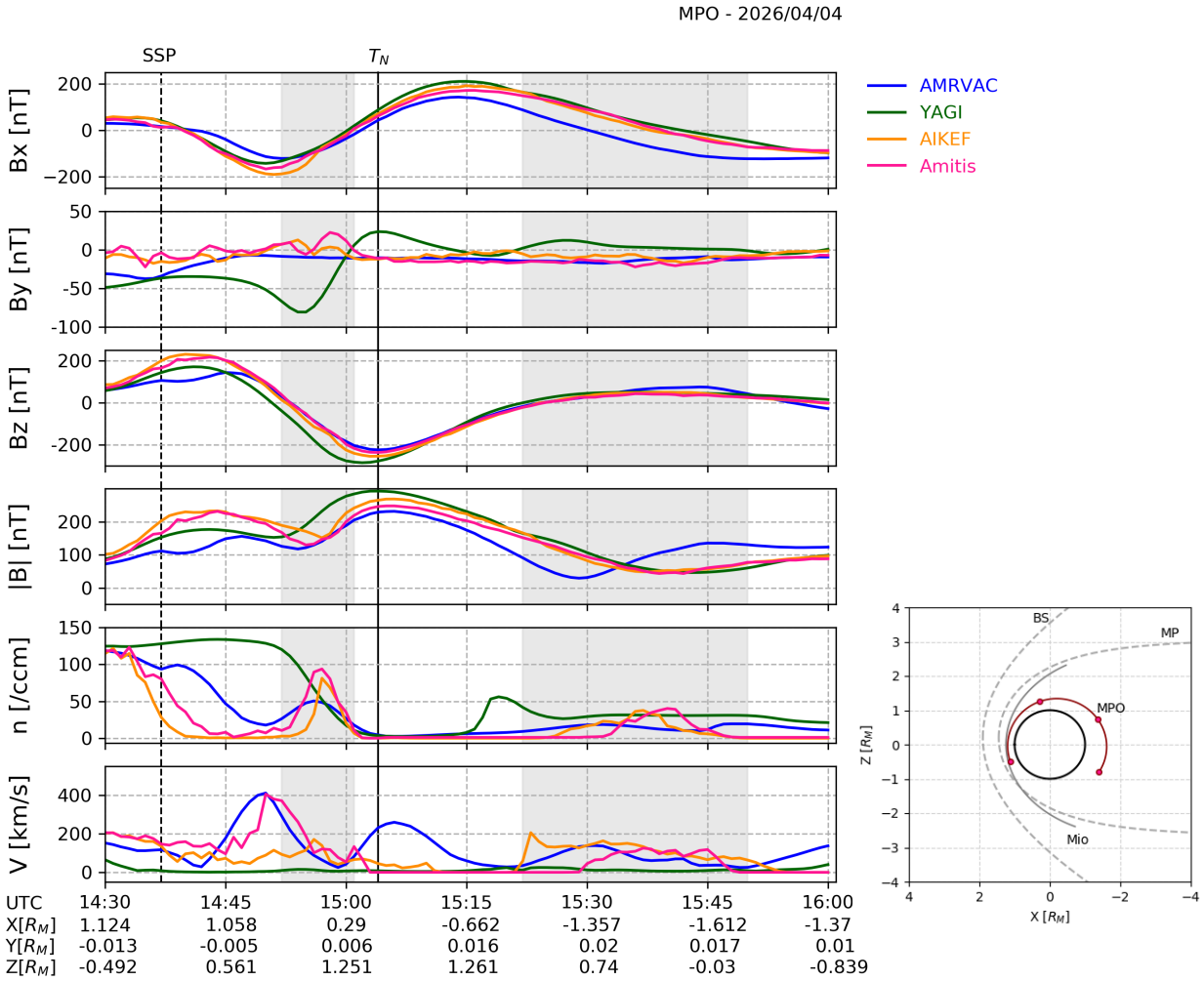

Figure 7: Magnetic field and particle data along a representative MPO orbit. The red dots along the trajectory in the inset panel show the position of the spacecraft along 30 min intervals. The solid vertical lines indicate northern (T_N) terminator and the dashed vertical line is the time when the spacecraft crosses the subsolar point (SSP).

6. Conclusions

We have compared the results of four different (MHD and hybrid) simulation models with the same input parameters to predict the solar wind interaction with Mercury's magnetosphere. All our models produced a similar global structure consistent with analytical model for the locations of the bow shock and the magnetopause. We note that small differences between the model predictions seem to be caused by the manner the planetary boundary conditions are implemented, rather than by having self-consistent ion kinetics included in the model.

We cross-compared our results with a theoretical northward IMF scenario (Case a) and MESSENGER orbit 1415 (Case b), indicated to have stable solar wind conditions with a northward IMF similar to the theoretical case. In Case a, the standard deviations for the predicted mean locations of the bow shock, magnetopause and the thickness of magnetosheath are small. For Case b, during the inbound part of the orbit, time differences for the bow shock and the magnetopause crossings are found up to 12 minutes, corresponding to a distance along the orbit of $0.28\,\mathrm{R_M}$. For the outbound section of the orbit, the maximum time difference increased to 17 minutes, equivalent to $1.1\,\mathrm{R_M}$.

One of the major goals of SHOTS is to prepare a catalog of simulations that can predict the plasma environment in- and outside the Hermean magnetosphere under different solar wind conditions, in this way contributing to maximizing the scientific return of the forthcoming BepiColombo observa-

tions. Here, for the first time, we have extracted the data from our models along representative Mio and MPO orbits. A long-lasting project-based and community-wide effort will be important both for the forthcoming Bepi-Colombo's Mercury flybys and during its nominal orbital phase.

Acknowledgments

The authors acknowledge support from the French space plasma physics data centre (Centre de Données de la Physique des Plasmas, CDPP: http://www.cdpp.eu funded by CNES and CNRS). J.D. acknowledges support from NASA's Solar System Exploration Research Virtual Institute (SSERVI): Institute for Modeling Plasmas, Atmosphere, and Cosmic Dust (IMPACT), and the NASA High-End Computing (HEC) Program through the NASA Advanced Supercomputing (NAS) Division at Ames Research Center. D.H. was supported by the German Ministerium für Wirtschaft und Energie and the German Zen- trum für Luft-und Raumfahrt under contract 50 QW 1501. W.E. was supported by DFG (German Research Foundation) under contract HE8016/1-1. S.F. acknowledges support from Swedish National Research Council, grant #2018- 03454, Swedish National Space Agency, grants #2018-C and #2018-N. Amitis simulations conducted using computational resources provided by the Swedish National Infrastructure for Computing (SNIC), projects SNIC2019/3-178 and SNIC2020-5-101 at the High Performance Computing Center North (HPC2N), Umeå University, Sweden. French co-authors would like to acknowledge the support of CNES for the BepiColombo mission. Part of this work has been done in the framework of

the Sun Planet Interactions Digital Environment on Request (SPIDER) activities of the Europlanet 2024 RI project. Europlanet 2024 RI has received funding from the European Union's Horizon 2020 research and innovation programme under grant agreement No 871149.

All data necessary to validate the findings presented in this manuscript can be found at `https://github.com/jandeca/Aizawa_etal_PSS_2020` (DOI: to be provided) in accordance with the FAIR principles. The magnetometer data from the MESSENGER observations are available in the Planetary Data System.

References

[1] N. F. Ness, K. W. Behannon, R. P. Lepping, Y. C. Whang, The magnetic field of mercury, 1, Journal of Geophysical Research (1896-1977) 80 (1975) 2708–2716. doi:10.1029/JA080i019p02708.

[2] Y. C. Whang, Magnetospheric magnetic field of mercury, Journal of Geophysical Research (1896-1977) 82 (1977) 1024–1030. doi:10.1029/JA082i007p01024.

[3] H. Korth, B. J. Anderson, C. L. Johnson, J. A. Slavin, J. M. Raines, T. H. Zurbuchen, Structure and configuration of mercury's magnetosphere, in: S. C. Solomon, L. R. Nittler, B. J. Anderson (Eds.), Mercury: The View after MESSENGER, Cambridge University Press, 2018, pp. 430–460.

[4] J. A. Slavin, D. N. Baker, D. J. Gershman, G. C. Ho, S. M. Imber, S. M. Krimigis, T. Sundberg, Mercury's dynamic magnetosphere, in: S. C. Solomon, L. R. Nittler, B. J. Anderson (Eds.), Mercury: The View after MESSENGER, Cambridge University Press, 2018, pp. 461–496.

[5] E. Jang, J. T. Zhao, C. Yue, Q. G. Zong, Y. Liu, Z. Y. Liu, Energetic Ion Dynamics Near the Cusp Region of Mercury, The Astrophysical Journal 892 (2020) 10. doi:10.3847/1538-4357/ab74d1.

[6] R. M. Winslow, B. J. Anderson, C. L. Johnson, J. A. Slavin, H. Korth, M. E. Purucker, D. N. Baker, S. C. Solomon, Mercury's magnetopause and bow shock from MESSENGER Magnetometer observations, Journal of Geophysical Research (Space Physics) 118 (2013) 2213–2227. doi:10.1002/jgra.50237.

[7] J. A. Slavin, G. A. DiBraccio, D. J. Gershman, S. M. Imber, G. K. Poh, J. M. Raines, T. H. Zurbuchen, X. Jia, D. N. Baker, K.-H. Glassmeier, S. A. Livi, S. A. Boardsen, T. A. Cassidy, M. Sarantos, T. Sundberg, A. Masters, C. L. Johnson, R. M. Winslow, B. J. Anderson, H. Korth, R. L. McNutt Jr., S. C. Solomon, Messenger observations of mercury's dayside magnetosphere under extreme solar wind conditions, Journal of Geophysical Research: Space Physics 119 (2014) 8087–8116. doi:10.1002/2014JA020319.

[8] J. A. Slavin, H. R. Middleton, J. M. Raines, X. Jia, J. Zhong, W.-J. Sun, S. Livi, S. M. Imber, G.-K. Poh, M. Akhavan-Tafti, J. M. Jasinski, G. A. DiBraccio, C. Dong, R. M. Dewey, M. L. Mays, Messenger observations of disappearing dayside magnetosphere events at mercury, Journal of

Geophysical Research: Space Physics 124 (2019) 6613–6635. doi:10.1029/2019JA026892.

[9] R. M. Winslow, N. Lugaz, L. Philpott, C. J. Farrugia, C. L. Johnson, B. J. Anderson, C. S. Paty, N. A. Schwadron, M. A. Asad, Observations of Extreme ICME Ram Pressure Compressing Mercury's Dayside Magnetosphere to the Surface, The Astrophysical Journal 889 (2020) 184. doi:10.3847/1538-4357/ab6170. arXiv:1903.00577.

[10] E. Kallio, P. Wurz, R. Killen, S. McKenna-Lawlor, A. Milillo, A. Mura, S. Massetti, S. Orsini, H. Lammer, P. Janhunen, On the impact of multiply charged heavy solar wind ions on the surface of Mercury, the Moon and Ceres, Planetary and Space Science 56 (2008) 1506–1516. doi:10.1016/j.pss.2008.07.018.

[11] J. M. Raines, D. J. Gershman, J. A. Slavin, T. H. Zurbuchen, H. Korth, B. J. Anderson, S. C. Solomon, Structure and dynamics of Mercury's magnetospheric cusp: MESSENGER measurements of protons and planetary ions, Journal of Geophysical Research (Space Physics) 119 (2014) 6587–6602. doi:10.1002/2014JA020120.

[12] S. Fatemi, A. R. Poppe, S. Barabash, Hybrid simulations of solar wind proton precipitation to the surface of mercury, Journal of Geophysical Research: Space Physics 125 (2020) e2019JA027706. doi:10.1029/2019JA027706.

[13] X. Jia, J. A. Slavin, T. I. Gombosi, L. K. S. Daldorff, G. Toth, B. van der Holst, Global MHD simulations of Mercury's magnetosphere with

coupled planetary interior: Induction effect of the planetary conducting core on the global interaction, Journal of Geophysical Research (Space Physics) 120 (2015) 4763–4775. doi:10.1002/2015JA021143.

[14] C. L. Johnson, L. C. Philpott, B. J. Anderson, H. Korth, S. A. Hauck, D. Heyner, R. J. Phillips, R. M. Winslow, S. C. Solomon, MESSENGER observations of induced magnetic fields in Mercury's core, Geophysical Research Letters 43 (2016) 2436–2444. doi:10.1002/2015GL067370.

[15] K. Kabin, T. Gombosi, D. DeZeeuw, K. Powell, Interaction of mercury with the solar wind, Icarus 143 (2000) 397 – 406. doi:http://dx.doi.org/10.1006/icar.1999.6252.

[16] M. Benna, B. J. Anderson, D. N. Baker, S. A. Boardsen, G. Gloeckler, R. E. Gold, G. C. Ho, R. M. Killen, H. Korth, S. M. Krimigis, M. E. Purucker, R. L. McNutt, J. M. Raines, W. E. McClintock, M. Sarantos, J. A. Slavin, S. C. Solomon, T. H. Zurbuchen, Modeling of the magnetosphere of Mercury at the time of the first MESSENGER flyby, Icarus 209 (2010) 3–10. doi:10.1016/j.icarus.2009.11.036.

[17] X. Jia, J. A. Slavin, T. I. Gombosi, L. K. S. Daldorff, G. Toth, B. van der Holst, Global mhd simulations of mercury's magnetosphere with coupled planetary interior: Induction effect of the planetary conducting core on the global interaction, Journal of Geophysical Research: Space Physics 120 (2015) 4763–4775. doi:10.1002/2015JA021143.

[18] C. Dong, L. Wang, A. Hakim, A. Bhattacharjee, J. A. Slavin, G. A. DiBraccio, K. Germaschewski, Global Ten-Moment Multifluid Simu-

588 lations of the Solar Wind Interaction with Mercury: From the Plan-
589 etary Conducting Core to the Dynamic Magnetosphere, Geophysical
590 Research Letters 46 (2019) 11,584–11,596. doi:10.1029/2019GL083180.
591 arXiv:1904.02695.

592 [19] E. Kallio, P. Janhunen, Modelling the solar wind interaction with Mer-
593 cury by a quasi-neutral hybrid model, Annales Geophysicae 21 (2003)
594 2133–2145. doi:10.5194/angeo-21-2133-2003.

595 [20] P. Trávníček, P. Hellinger, D. Schriver, Structure of Mercury's magne-
596 tosphere for different pressure of the solar wind: Three dimensional
597 hybrid simulations, Geophysical Research Letters 34 (2007) 5104.
598 doi:10.1029/2006GL028518.

599 [21] P. M. Trávníček, D. Schriver, P. Hellinger, D. Herčík, B. J. An-
600 derson, M. Sarantos, J. A. Slavin, Mercury's magnetosphere: so-
601 lar wind interaction for northward and southward interplanetary mag-
602 netic field: Hybrid simulation results, Icarus 209 (2010) 11 – 22.
603 doi:http://dx.doi.org/10.1016/j.icarus.2010.01.008.

604 [22] Y.-C. Wang, J. Mueller, U. Motschmann, W.-H. Ip, A hybrid simulation
605 of Mercury's magnetosphere for the MESSENGER encounters in year
606 2008, Icarus 209 (2010) 46–52. doi:10.1016/j.icarus.2010.05.020.

607 [23] D. Herčík, P. M. Trávníček, J. R. Johnson, E.-H. Kim, P. Hellinger, Mir-
608 ror mode structures in the asymmetric hermean magnetosheath: Hybrid
609 simulations, Journal of Geophysical Research: Space Physics 118 (2013)
610 405–417. doi:10.1029/2012JA018083.

[24] S. Fatemi, A. R. Poppe, G. T. Delory, W. M. Farrell, Amitis: A 3d gpu-based hybrid-pic model for space and plasma physics, Journal of Physics: Conference Series 837 (2017) 012017.

[25] S. Fatemi, N. Poirier, M. Holmström, J. Lindkvist, M. Wieser, S. Barabash, A modelling approach to infer the solar wind dynamic pressure from magnetic field observations inside Mercury's magnetosphere, Astronomy & Astrophysics 614 (2018) A132. doi:10.1051/0004-6361/201832764.

[26] W. Exner, D. Heyner, L. Liuzzo, U. Motschmann, D. Shiota, K. Kusano, T. Shibayama, Coronal mass ejection hits mercury: A.i.k.e.f. hybrid-code results compared to messenger data, Planetary and Space Science 153 (2018) 89 – 99.

[27] J. Müller, S. Simon, Y.-C. Wang, U. Motschmann, D. Heyner, J. Schüle, W.-H. Ip, G. Kleindienst, G. J. Pringle, Origin of Mercury's double magnetopause: 3D hybrid simulation study with A.I.K.E.F., Icarus 218 (2012) 666–687. doi:10.1016/j.icarus.2011.12.028.

[28] J. A. Slavin, M. H. Acuña, B. J. Anderson, D. N. Baker, M. Benna, G. Gloeckler, R. E. Gold, G. C. Ho, R. M. Killen, H. Korth, S. M. Krimigis, R. L. McNutt, L. R. Nittler, J. M. Raines, D. Schriver, S. C. Solomon, R. D. Starr, P. Trávníček, T. H. Zurbuchen, Mercury's Magnetosphere After MESSENGER's First Flyby, Science 321 (2008) 85–89. doi:10.1126/science.1159040.

[29] B. J. Anderson, J. A. Slavin, H. Korth, S. A. Boardsen, T. H. Zurbuchen,

J. M. Raines, G. Gloeckler, R. L. McNutt, S. C. Solomon, The dayside magnetospheric boundary layer at Mercury, Planetary and Space Science 59 (2011) 2037–2050. doi:10.1016/j.pss.2011.01.010.

[30] I. B. Peng, S. Markidis, E. Laure, A. Johlander, A. Vaivads, Y. Khotyaintsev, P. Henri, G. Lapenta, Kinetic structures of quasi-perpendicular shocks in global particle-in-cell simulations, Physics of Plasmas 22 (2015) 092109. doi:10.1063/1.4930212.

[31] I. B. Peng, S. Markidis, A. Vaivads, J. Vencels, J. Amaya, A. Divin, E. Laure, G. Lapenta, The formation of a magnetosphere with implicit particle-in-cell simulations, Procedia Computer Science 51 (2015) 1178 – 1187. doi:http://dx.doi.org/10.1016/j.procs.2015.05.288, international Conference On Computational Science 2015: Computational Science at the Gates of Nature.

[32] Y. Chen, G. Toth, X. Jia, J. Slavin, W. Sun, S. Markidis, T. Gombosi, J. Raines, Studying dawn-dusk asymmetries of mercury's magnetotail using mhd-epic simulations, Journal of Geophysical Research: Space Physics (Submitted) (2019).

[33] T. Mukai, H. Yamakawa, H. Hayakawa, Y. Kasaba, H. Ogawa, Present status of the bepicolombo/mercury magnetospheric orbiter, Advances in Space Research 38 (2006) 578 – 582. doi:https://doi.org/10.1016/j.asr.2005.09.038, mercury, Mars and Saturn.

[34] A. Milillo, M. Fujimoto, E. Kallio, S. Kameda, F. Leblanc, Y. Narita, G. Cremonese, H. Laakso, M. Laurenza, S. Massetti, S. McKenna-

Lawlor, A. Mura, R. Nakamura, Y. Omura, D. A. Rothery, K. Seki, M. Storini, P. Wurz, W. Baumjohann, E. J. Bunce, Y. Kasaba, J. Helbert, A. Sprague, Hermean Environment WG members, The Bepi-Colombo mission: An outstanding tool for investigating the Hermean environment, Planetary and Space Science 58 (2010) 40–60. doi:10.1016/j.pss.2008.06.005.

[35] B. J. Anderson, C. L. Johnson, H. Korth, R. M. Winslow, J. E. Borovsky, M. E. Purucker, J. a. Slavin, S. C. Solomon, M. T. Zuber, R. L. McNutt, Low-degree structure in Mercury's planetary magnetic field, Journal of Geophysical Research E: Planets 117 (2012) 1–17. doi:10.1029/2012JE004159.

[36] R. Keppens, Z. Meliani, A. J. van Marle, P. Delmont, A. Vlasis, B. van der Holst, Parallel, grid-adaptive approaches for relativistic hydro and magnetohydrodynamics, Journal of Computational Physics 231 (2012) 718–744. doi:10.1016/j.jcp.2011.01.020.

[37] C. Xia, J. Teunissen, I. E. Mellah, E. Chané, R. Keppens, MPI-AMRVAC 2.0 for solar and astrophysical applications, The Astrophysical Journal Supplement Series 234 (2018) 30. doi:10.3847/1538-4365/aaa6c8.

[38] K. G. Powell, P. L. Roe, T. J. Linde, T. I. Gombosi, D. L. De Zeeuw, A Solution-Adaptive Upwind Scheme for Ideal Magnetohydrodynamics, Journal of Computational Physics 154 (1999) 284–309. doi:10.1006/jcph.1999.6299.

[39] L. Griton, F. Pantellini, Z. Meliani, Three-dimensional magnetohydrodynamic simulations of the solar wind interaction with a hyperfast-rotating uranus, Journal of Geophysical Research: Space Physics 123 (2018) 5394–5406. doi:10.1029/2018JA025331.

[40] M. Yagi, K. Seki, Y. Matsumoto, Development of a magnetohydrodynamic simulation code satisfying the solenoidal magnetic field condition, Computer Physics Communications 180 (2009) 1550 – 1557. doi:https://doi.org/10.1016/j.cpc.2009.04.010.

[41] M. Yagi, K. Seki, Y. Matsumoto, D. C. Delcourt, F. Leblanc, Formation of a sodium ring in mercury's magnetosphere, Journal of Geophysical Research: Space Physics 115 (2010). doi:10.1029/2009JA015226.

[42] J. Müller, S. Simon, U. Motschmann, J. Schüle, K.-H. Glaßmeier, G. J. Pringle, A.i.k.e.f.: Adaptive hybrid model for space plasma simulations, Computer Physics Communications 182 (2011) 946–966. doi:10.1016/j.cpc.2010.12.033.

[43] J. Müller, S. Simon, Y.-C. Wang, U. Motschmann, D. Heyner, J. Schüle, W.-H. Ip, G. Kleindienst, G. J. Pringle, Origin of mercury's double magnetopause: 3d hybrid simulation study with a.i.k.e.f., Icarus 218 (2012) 666 – 687. doi:https://doi.org/10.1016/j.icarus.2011.12.028.

[44] C. Jacquey, V. Génot, E. Budnik, R. Hitier, M. Bouchemit, M. Gangloff, A. Fedorov, B. Cecconi, N. André, B. Lavraud, C. Harvey, F. Dériot, D. Heulet, E. Pallier, E. Penou, J. L. Pinçon, AMDA, Auto-

mated Multi-Dataset Analysis: A Web-Based Service Provided by the CDPP, Astrophysics and Space Science Proceedings 11 (2010) 239–247. doi:10.1007\/978-90-481-3499-1_16.

[45] V. Génot, C. Jacquey, M. Bouchemit, M. Gangloff, A. Fedorov, B. Lavraud, N. André, L. Broussillou, C. Harvey, E. Pallier, E. Penou, E. Budnik, R. Hitier, B. Cecconi, F. Dériot, D. Heulet, J. L. Pinçon, Space Weather applications with CDPP/AMDA, Advances in Space Research 45 (2010) 1145–1155. doi:10.1016/j.asr.2009.11.010.

[46] V. Génot, L. Beigbeder, D. Popescu, N. Dufourg, M. Gangloff, M. Bouchemit, S. Caussarieu, J. P. Toniutti, J. Durand, R. Modolo, N. André, B. Cecconi, C. Jacquey, F. Pitout, A. Rouillard, R. Pinto, S. Erard, N. Jourdane, L. Leclercq, S. Hess, M. Khodachenko, T. Al-Ubaidi, M. Scherf, E. Budnik, Science data visualization in planetary and heliospheric contexts with 3DView, Planetary and Space Science 150 (2018) 111–130. doi:10.1016/j.pss.2017.07.007.

[47] D. A. Roberts, J. Thieman, V. Génot, T. King, M. Gangloff, C. Perry, C. Wiegand , D. De Zeeuw, S. F. Fung, B. Cecconi, S. Hess, The SPASE Data Model: A Metadata Standard for Registering, Finding, Accessing, and Using Heliophysics Data Obtained From Observations and Modeling, Space Weather 16 (2018) 1899–1911. doi:10.1029/2018SW002038.

[48] M. Sarantos, P. H. Reiff, T. W. Hill, R. M. Killen, A. L. Urquhart, A B_x-interconnected magnetosphere model for Mercury, Planetary and Space Science 49 (2001) 1629–1635. doi:10.1016/S0032-0633(01)00100-3.

[49] B. J. Anderson, C. L. Johnson, H. Korth, A magnetic disturbance index for Mercury's magnetic field derived from MESSENGER Magnetometer data, Geochemistry, Geophysics, Geosystems 14 (2013) 3875–3886. doi:10.1002/ggge.20242.

[50] E. Marsch, R. Schwenn, H. Rosenbauer, K. H. Muehlhaeuser, W. Pilipp, F. M. Neubauer, Solar wind protons: Three-dimensional velocity distributions and derived plasma parameters measured between 0.3 and 1 AU, Journal of Geophysical Research 87 (1982) 52–72. doi:10.1029/JA087iA01p00052.

[51] I. Wilson, Lynn B., M. L. Stevens, J. C. Kasper, K. G. Klein, B. A. Maruca, S. D. Bale, T. A. Bowen, M. P. Pulupa, C. S. Salem, The Statistical Properties of Solar Wind Temperature Parameters Near 1 au, The Astrophysical Journal Supplement Series 236 (2018) 41. doi:10.3847/1538-4365/aab71c. arXiv:1802.08585.

[52] J. A. Slavin, M. H. Acuña, B. J. Anderson, D. N. Baker, M. Benna, S. A. Boardsen, G. Gloeckler, R. E. Gold, G. C. Ho, H. Korth, S. M. Krimigis, R. L. McNutt, J. M. Raines, M. Sarantos, D. Schriver, S. C. Solomon, P. Trávníček, T. H. Zurbuchen, Messenger observations of magnetic reconnection in mercury's magnetosphere, Science 324 (2009) 606–610. doi:10.1126/science.1172011.

[53] J. H. Shue, J. K. Chao, H. C. Fu, C. T. Russell, P. Song, K. K. Khurana, H. J. Singer, A new functional form to study the solar wind control of the magnetopause size and shape, Journal of Geophysical Research (Space Physics) 102 (1997) 9497–9512. doi:10.1029/97JA00196.

[54] W. Baumjohann, A. Matsuoka, W. Magnes, K.-H. Glassmeier, R. Nakamura, H. Biernat, M. Delva, K. Schwingenschuh, T. Zhang, H.-U. Auster, K.-H. Fornacon, I. Richter, A. Balogh, P. Cargill, C. Carr, M. Dougherty, T. S. Horbury, E. A. Lucek, F. Tohyama, T. Takahashi, M. Tanaka, T. Nagai, H. Tsunakawa, M. Matsushima, H. Kawano, A. Yoshikawa, H. Shibuya, T. Nakagawa, M. Hoshino, Y. Tanaka, R. Kataoka, B. J. Anderson, C. T. Russell, U. Motschmann, M. Shinohara, Magnetic field investigation of Mercury's magnetosphere and the inner heliosphere by MMO/MGF, Planetary and Space Science 58 (2010) 279–286. doi:10.1016/j.pss.2008.05.019.

[55] K. H. Glassmeier, H. U. Auster, D. Heyner, K. Okrafka, C. Carr, G. Berghofer, B. J. Anderson, A. Balogh, W. Baumjohann, P. Cargill, U. Christensen, M. Delva, M. Dougherty, K. H. Fornaçon, T. S. Horbury, E. A. Lucek, W. Magnes, M. Mandea, A. Matsuoka, M. Matsushima, U. Motschmann, R. Nakamura, Y. Narita, H. O'Brien, I. Richter, K. Schwingenschuh, H. Shibuya, J. A. Slavin, C. Sotin, B. Stoll, H. Tsunakawa, S. Vennerstrom, J. Vogt, T. Zhang, The fluxgate magnetometer of the BepiColombo Mercury Planetary Orbiter, Planetary and Space Science 58 (2010) 287–299. doi:10.1016/j.pss.2008.06.018.

[56] Y. Saito, J. Sauvaud, M. Hirahara, S. Barabash, D. Delcourt, T. Takashima, K. Asamura, Scientific objectives and instrumentation of mercury plasma particle experiment (mppe) onboard mmo, Planetary and Space Science 58 (2010) 182 – 200. doi:https://doi.org/10.1016/j.pss.2008.06.003, comprehensive Science Investigations of Mercury:

The scientific goals of the joint ESA/JAXA mission BepiColombo.

[57] Y. Kasaba, J.-L. Bougeret, L. Blomberg, H. Kojima, S. Yagitani, M. Moncuquet, J.-G. Trotignon, G. Chanteur, A. Kumamoto, Y. Kasahara, J. Lichtenberger, Y. Omura, K. Ishisaka, H. Matsumoto, The plasma wave investigation (pwi) onboard the bepicolombo/mmo: First measurement of electric fields, electromagnetic waves, and radio waves around mercury, Planetary and Space Science 58 (2010) 238 – 278. doi:https://doi.org/10.1016/j.pss.2008.07.017, comprehensive Science Investigations of Mercury: The scientific goals of the joint ESA/JAXA mission BepiColombo.

[58] S. Orsini, S. Livi, K. Torkar, S. Barabash, A. Milillo, P. Wurz, A. M. di Lellis, E. Kallio, SERENA Team, SERENA: A suite of four instruments (ELENA, STROFIO, PICAM and MIPA) on board BepiColombo-MPO for particle detection in the Hermean environment, Planetary and Space Science 58 (2010) 166–181. doi:10.1016/j.pss.2008.09.012.